THE ASTRONOMICAL JOURNAL VOLUME 112, NUMBER 5 NOVEMBER 1996

COLOR DIVERSITY AMONG THE CENTAURS AND KUIPER BELT OBJECTS

JANE LUU[1,2]

Astronomy Department, Harvard University, Cambridge, Massachusetts 02138
Electronic mail: luu@cfa.harvard.edu

DAVID JEWITT[1,2]

Institute for Astronomy, University of Hawaii, 2680 Woodlawn Drive, Honolulu, Hawaii 96825
Electronic mail: jewitt@galileo.ifa.hawaii.edu

Received 1996 April 11; revised 1996 July 17

ABSTRACT

We present new broadband optical photometry of Centaurs and Kuiper Belt objects from the Keck 10 m, the University of Hawaii 2.2 m, and the Cerro Tololo InterAmerican Observatory (CTIO) 1.5 m telescopes. These objects are believed to represent large protocomets in different stages of dynamical evolution. We find a wide dispersion in the optical colors of the objects, indicating nonuniform surface properties. The color dispersion must be understood in the context of the expected steady reddening due to bombardment by the ubiquitous flux of cosmic rays. We describe a model in which the dispersion is produced by stochastic collisional resurfacing. While non-unique, this model provides a plausible match to the observed color spread.

1. INTRODUCTION

Until recently, the only known permanent residents of the outer solar system were the distant planets and their satellites. Ongoing observational surveys have revealed an abundance of interplanetary bodies that previously escaped notice due to their faintness (Jewitt & Luu 1995; Irwin *et al.* 1995; Williams *et al.* 1995, Jewitt *et al.* 1996). These so-called Kuiper Belt objects orbit beyond Neptune. They are thought to be relics from the formation phase of the solar system and are widely believed to represent the source region of the short-period comets (Duncan *et al.* 1988). The Centaurs are a dynamically separate family of objects on unstable orbits whose semimajor axes fall between those of Jupiter and Neptune. Centaurs may be bodies dislodged from the Kuiper Belt region and are in the process of being scattered by the planets. Their dynamical lifetimes are measured in millions of years (Hahn & Bailey 1990; Asher & Steel 1993), clearly separating them from the much more stable objects in the Kuiper Belt (e.g., Holman & Wisdom 1993).

Kuiper Belt objects are believed to possess interiors rich in abundant molecular ices (water, carbon dioxide, carbon monoxide, diatomic nitrogen), commensurate with their accumulation in the outer regions of the solar nebula at temperatures of perhaps only 40–50 K. Prolonged cosmic-ray irradiation of initially ice-rich material may transmute near-surface volatiles into more complex, polymerized forms. Laboratory experiments show that bombardment of astrophysical ice mixtures (such as H_2O, NH_3, CH_4) by high-energy particles results in the selective loss of hydrogen and the formation of carbon residues (Moore *et al.* 1983). The so-called "irradiation mantle" which results from long-term irradiation is a carbon-rich, refractory solid which inhibits sublimation of ices buried underneath. This dark, involatile mantle is expected to cover most of the Kuiper Belt objects, and perhaps also the Centaurs, if the latter are indeed escapees from the Kuiper Belt.

Pluto, the largest known Kuiper Belt object, tells us little about the surface composition of the rest of the Kuiper Belt population, since its surface is continually modified by interaction with its atmosphere. Pluto's satellite, Charon, may be a better representative but we possess few data on the surface nature of this body.

In this paper we take a first step toward the investigation of the physical properties of Kuiper Belt objects. We present new optical observations of these bodies and discuss them in terms of their surface compositions and their possible connections with other solar system objects. Our observations were obtained using fixed observing and data-reduction procedures, thus reducing possible errors due to systematic effects. Nevertheless, the Kuiper Belt objects are very faint, and the determination of their optical colors presents a formidable observational challenge.

TABLE 1. Instrumental parameters.

Telescope	Diameter [m]	Detector Size [pixels]	Pixel Size [arcsec]	Typical Seeing [arcsec]
Keck I	10	2048x2048	0.22	0.7 - 1.0
UH	2.2	2048x2048	0.22	0.7 - 1.0
CTIO	1.5	2048x2048	0.43	0.9 - 1.3

[1]Visiting Astronomer, W. M. Keck Observatory, jointly operated by California Institute of Technology and the University of California.
[2]Visiting Astronomer, Cerro Tololo Interamerican Observatory, National Optical Astronomy Observatories, operated by the Association of Universities for Research in Astronomy Inc., under contract with the National Science Foundation.

 0004-6256/96/112(5)/2310/9/$10.00

TABLE 2. Effective central wavelengths of filters.

Filter	Central wavelength λ_c [Å]	Filter bandpass [Å]
B	4500	1200
V	5400	1000
R	6500	1200
I	8400	2000

2. OBSERVATIONS

Observations were taken using the Keck 10 m telescope, the University of Hawaii (UH) 2.2 m telescope, both on Mauna Kea, Hawaii, and the Cerro Tololo InterAmerican Observatory (CTIO) 1.5 m telescope in Chile. On the Keck telescope we used the low-resolution imaging spectrometer (LRIS) in imaging mode (Oke *et al.* 1995) while at the other telescopes we used dedicated imaging cameras. Instrumental parameters are summarized in Table 1. Pixel-to-pixel variations in the images were removed by subtracting the bias level then dividing by a "flat field," created from median-stacked offset images of the twilight sky. After processing, the images were uniform in sensitivity to better than 0.5% across the full width of the CCD, and substantially better on smaller scales. Nearby standard stars (Landolt 1992) were observed throughout each night for the purpose of photometric calibration.

The telescopes were tracked at sidereal rate, and during our integrations ($\leq$900 s), the targets trailed less than 0.″8. All observations were made through broadband Mould *BVRI* filters, and integration times were varied according to the brightness of each object. The effective central wavelengths for the filters are listed in Table 2. Depending on the seeing, the nightly photometry apertures ranged from 1.1 to 1.5 arcsec in radius; in particular, all the Keck photometry was computed with a 1.5 arcsec radius. Sky subtraction was performed by measuring and subtracting the sky background in an annulus with an 1.5 arcsec inner radius and a 3.3 arcsec outer radius. Photometric errors are due mainly to uncertainty in the level of the night sky background, caused by faint field galaxies and stars. Images clearly affected by background objects were rejected from the present study. In some cases, background sources may be present at the limits of detection; their effect is best judged from the scatter in the

TABLE 3. Orbital characteristics.†

Object	Class	a [a] [AU]	e [b]	i [c] [deg]
2060 Chiron	Centaur	13.7	0.38	6.9
5145 Pholus	Centaur	20.4	0.57	24.7
1993 HA_2	Centaur	24.8	0.52	15.6
1995 DW_2	Centaur	24.2	0.22	4.2
1992 QB_1	Kuiper Belt	44.0	0.07	2.2
1993 FW	Kuiper Belt	43.8	0.05	7.8
1993 RO	Kuiper Belt	39.4	0.20	3.7
1993 SC	Kuiper Belt	39.7	0.19	5.1
1994 ES_2	Kuiper Belt	46.0	0.13	1.1
1994 EV_3	Kuiper Belt	43.0	0.04	1.7
1994 JS	Kuiper Belt	42.9	0.24	14.0
1994 JV	Kuiper Belt	42.4	0.20	15.7
1994 TB	Kuiper Belt	39.3	0.31	12.1
1995 DA_2	Kuiper Belt	36.3	0.11	6.6
1995 DB_2	Kuiper Belt	43.4	0.07	4.3
1995 DC_2	Kuiper Belt	45.1	0.00	2.1
1995 QY_9	Kuiper Belt	39.4	0.25	4.8
1995 WY_2	Kuiper Belt	48.2	0.00	10.2

† Orbital elements by Brian Marsden, Center for Astrophysics
[a] Semimajor axis
[b] Eccentricity
[c] Inclination

TABLE 4. (a) Observation log—Centaurs.

Object	Date	R [a] [AU]	Δ [b] [AU]	α [c] [deg]	Telescope	Filter
2060 Chiron	1991 Sep 12	10.17	10.88	-3.9	UH 2.2m	V, R
	1991 Sep 14	10.16	10.85	-4.0	UH 2.2m	B, V, R
	1992 Nov 27	9.44	9.19	-5.9	UH 2.2m	R
	1994 May 18	8.77	8.60	6.6	CTIO 1.5m	B, V, R, I
5145 Pholus	1992 Nov 27	8.89	8.57	-6.1	UH 2.2m	R
	1993 Mar 27	9.02	8.39	5.1	UH 2.2m	V, R
1993 HA_2	1993 Jul 17	11.97	11.79	4.8	UH 2.2m	B, V, R, I
	1994 May 16	12.19	11.20	0.9	CTIO 1.5m	B, V, R, I
	1995 Mar 24	12.50	11.90	-3.7	Keck	B, V, R
1995 DW_2	1995 Mar 23	18.89	17.90	-0.1	Keck	B, V, R

[a] Heliocentric distance
[b] Geocentric distance
[c] Phase angle

TABLE 4. (b) Observation log—Kuiper Belt objects.

Object	Date	R [a] [AU]	Δ [b] [AU]	α [c] [deg]	Telescope	Filter
1992 QB_1	1992 Aug 30	40.88	39.95	-0.6	UH 2.2m	R
	1992 Sep 01	40.88	39.93	-0.5	UH 2.2m	R, I
	1993 Sep 13	40.88	39.88	-0.2	UH 2.2m	B, V, R, I
	1993 Sep 17	40.88	39.88	-0.1	UH 2.2m	R, I
1993 FW	1993 Mar 28	42.16	41.16	0.0	UH 2.2m	V, R, I
	1993 Mar 29	42.16	41.16	0.0	UH 2.2m	R
	1995 Mar 23	42.09	41.11	-0.2	Keck	B, V, R
1993 RO	1993 Sep 14	31.55	30.54	0.1	UH 2.2m	B, V, R, I
	1993 Sep 15	31.55	30.54	0.1	UH 2.2m	B, V, R, I
	1993 Sep 16	31.55	30.54	0.1	UH 2.2m	V, R
	1993 Sep 17	31.55	30.54	0.2	UH 2.2m	R, I
1993 SC	1994 Sep 29	34.03	33.03	0.2	UH 2.2m	R, I
1994 ES_2	1995 Nov 19	45.64	45.87	-1.2	Keck	B, V, R, I
1994 EV_3	1994 May 15	44.65	43.84	0.8	CTIO 1.5m	R
	1995 Mar 24	44.66	43.70	-0.4	Keck	B, V, R
1994 JS	1994 May 14	36.03	35.02	-0.1	CTIO 1.5m	V, R
	1994 May 15	36.03	35.02	-0.1	CTIO 1.5m	R
1994 JV	1994 May 14	34.14	33.23	0.7	CTIO 1.5m	R, I
	1994 May 15	34.14	33.23	0.8	CTIO 1.5m	R, I
1994 TB	1995 Nov 19	30.94	30.51	1.7	Keck	B, V, R, I
1995 DA_2	1995 Mar 24	34.00	33.45	1.4	Keck	R
1995 DB_2	1995 Mar 24	40.57	40.00	1.2	Keck	R
1995 DC_2	1995 Mar 24	45.21	44.35	0.7	Keck	R
1995 QY_9	1995 Nov 19	29.91	29.68	1.9	Keck	B, V, R, I
1995 WY_2	1995 Nov 19	48.22	47.30	-0.5	Keck	B, V, R, I

[a] Heliocentric distance
[b] Geocentric distance
[c] Phase angle

TABLE 5. (a) Broadband photometry—Centaurs.

Object	Date	m_R[a]	H_R[b]	B-V	V-R	R-I
2060 Chiron	1991 Sep 12	15.86 ± 0.02	5.50 ± 0.02	–	0.31 ± 0.03	–
	1991 Sep 14	15.82 ± 0.03	5.47 ± 0.03	0.67 ± 0.06	0.42 ± 0.05	–
	1992 Nov 27	15.78 ± 0.03	5.91 ± 0.03	–	–	–
	1994 May 18	15.98 ± 0.02	6.39 ± 0.02	0.65 ± 0.05	0.37 ± 0.05	0.54 ± 0.10
5145 Pholus	1992 Nov 27	16.69 ± 0.05	6.80 ± 0.05	–		
	1993 Mar 27	16.49 ± 0.05	6.67 ± 0.05	–	0.84 ± 0.07	–
1993 HA_2	1993 Jul 17	20.09 ± 0.04	8.93 ± 0.04	0.88 ± 0.07	0.72 ± 0.05	0.66 ± 0.05
	1994 May 16	19.54 ± 0.03	8.72 ± 0.03	1.02 ± 0.08	0.81 ± 0.08	0.78 ± 0.10
	1995 Mar 24	19.89 ± 0.03	8.68 ± 0.03	1.18 ± 0.05	0.88 ± 0.05	–
1995 DW_2	1995 Mar 23	21.58 ± 0.04	8.90 ± 0.04	0.64 ± 0.04	0.51 ± 0.04	–

[a] Apparent R magnitude
[b] Absolute magnitude (as defined by Bowell *et al.* 1989)

TABLE 5. (b) Broadband photometry—Kuiper Belt objects.

Object	Date	m_R[a]	H_R[b]	B-V	V-R	R-I
1992 QB_1	1992 Aug 30	22.82 ± 0.10	6.64 ± 0.10	–	–	–
	1992 Sep 01	22.90 ± 0.20	6.74 ± 0.20	–	–	1.10 ± 0.30
	1993 Sep 13	22.64 ± 0.10	6.53 ± 0.10	0.65 ± 0.15	0.77 ± 0.15	0.64 ± 0.20
	1993 Sep 17	22.95 ± 0.10	6.85 ± 0.10	–	–	0.49 ± 0.20
1993 FW	1993 Mar 28	22.81 ± 0.12	6.61 ± 0.12	–	0.36 ± 0.16	0.50 ± 0.15
	1993 Mar 29	22.71 ± 0.15	6.51 ± 0.15	–	–	–
	1995 Mar 23	22.87 ± 0.04	6.62 ± 0.04	0.89 ± 0.05	0.64 ± 0.05	–
1993 RO	1993 Sep 14	23.29 ± 0.12	8.33 ± 0.12	0.87 ± 0.17	0.58 ± 0.17	0.25 ± 0.17
	1993 Sep 15	23.41 ± 0.10	8.45 ± 0.10	1.20 ± 0.17	0.43 ± 0.14	0.40 ± 0.14
	1993 Sep 16	23.31 ± 0.10	8.35 ± 0.10	–	0.67 ± 0.14	–
	1993 Sep 17	23.36 ± 0.10	8.38 ± 0.10	–	–	0.89 ± 0.14
1993 SC	1994 Sep 29	21.87 ± 0.05	6.56 ± 0.05	0.92 ± 0.11[c]	0.57 ± 0.09[c]	0.86 ± 0.10
1994 ES_2	1995 Nov 19	24.14 ± 0.10	7.36 ± 0.10	0.71 ± 0.15	0.94 ± 0.15	0.97 ± 0.15
1994 EV_3	1994 May 15	23.50 ± 0.06	6.91 ± 0.06	–	–	–
	1995 Mar 24	23.61 ± 0.03	7.07 ± 0.03	1.50 ± 0.15	0.54 ± 0.05	–
1994 JS	1994 May 14	22.74 ± 0.05	7.20 ± 0.05	–	0.85 ± 0.07	–
	1994 May 15	22.78 ± 0.07	7.24 ± 0.07	–	–	–
1994 JV	1994 May 14	22.64 ± 0.05	7.24 ± 0.05	–	0.81 ± 0.07	0.65 ± 0.07
	1994 May 15	22.58 ± 0.05	7.17 ± 0.05	–	0.72 ± 0.09	0.44 ± 0.10
1994 TB	1995 Nov 19	22.39 ± 0.03	7.30 ± 0.03	0.88 ± 0.15	0.85 ± 0.15	0.65 ± 0.15
1995 DA_2	1995 Mar 24	23.40 ± 0.04	7.93 ± 0.04	–	–	–
1995 DB_2	1995 Mar 24	24.14 ± 0.05	7.92 ± 0.05	–	–	–
1995 DC_2	1995 Mar 24	23.44 ± 0.05	6.81 ± 0.05	–	–	–
1995 QY_9	1995 Nov 19	22.43 ± 0.05	7.46 ± 0.05	0.68 ± 0.07	0.46 ± 0.06	0.40 ± 0.06
1995 WY_2	1995 Nov 19	23.56 ± 0.05	6.67 ± 0.05	0.99 ± 0.15	0.68 ± 0.15	0.43 ± 0.15

[a] Apparent R magnitude
[b] Absolute R magnitude (as defined by Bowell *et al.* 1989)
[c] Color computed from CCD spectrum

photometry from night to night. The telescopes and basic detector parameters are summarized in Table 1, the target objects and their orbital characteristics in Table 3, and the geometric circumstances at the times of observation in Table 4. The individual measurements are presented in Table 5.

3. RESULTS

A summary of the measurements is given in Table 6. Where separate measurements are available for a particular color, we have listed the weighted means. Within the uncertainties, our measurements are consistent with colors available in the literature (e.g., the brightest Centaurs Chiron and Pholus were independently measured by Hartmann *et al.* 1990 and Mueller *et al.* 1992).

The optical colors listed in Table 6 are all redder than sunlight, and show a dispersion larger than can be attributed

TABLE 6. Photometry summary.

Object	H_R	B-V	V-R	R-I
Centaurs				
2060 Chiron	5.82 ± 0.22	0.66 ± 0.04	0.35 ± 0.02	0.54 ± 0.10
			0.37 ± 0.02[a]	0.31 ± 0.02[a]
5145 Pholus	6.74 ± 0.07	1.35 ± 0.05[b]	0.84 ± 0.07	0.76 ± 0.06[b]
			0.75 ± 0.04[b]	
			0.81 ± 0.006[c]	
1993 HA_2	8.78 ± 0.08	1.09 ± 0.04	0.81 ± 0.03	0.69 ± 0.04
1995 DW_2	8.90 ± 0.04	0.64 ± 0.04	0.51 ± 0.04	----
Kuiper Belt Objects				
1992 QB_1	6.69 ± 0.07	0.65 ± 0.15	0.77 ± 0.30	0.74 ± 0.13
1993 FW	6.58 ± 0.04	0.89 ± 0.05	0.62 ± 0.05	0.50 ± 0.16
1993 RO	8.38 ± 0.03	1.07 ± 0.12	0.57 ± 0.09	0.65 ± 0.09
1993 SC	6.56 ± 0.05	0.92 ± 0.11	0.57 ± 0.09	0.86 ± 0.10
1994 ES_2	7.36 ± 0.10	0.71 ± 0.15	0.94 ± 0.15	0.97 ± 0.15
1994 EV_3	6.99 ± 0.08	1.50 ± 0.19	0.54 ± 0.05	----
1994 JS	7.22 ± 0.02	----	0.85 ± 0.07	----
1994 JV	7.25 ± 0.08	----	0.78 ± 0.06	0.59 ± 0.06
1994 TB	7.30 ± 0.03	0.88 ± 0.15	0.85 ± 0.15	0.65 ± 0.15
1995 DA_2	7.93 ± 0.04	----	----	----
1995 DB_2	7.92 ± 0.05	----	----	----
1995 DC_2	6.81 ± 0.05	----	----	----
1995 QY_9	7.46 ± 0.05	0.68 ± 0.07	0.46 ± 0.06	0.40 ± 0.06
1995 WY_2	6.67 ± 0.05	0.99 ± 0.15	0.68 ± 0.15	0.43 ± 0.15
Solar Colors[d]		0.67	0.36	0.33

[a] Hartmann *et al.* (1990)
[b] Mueller *et al.* (1992)
[c] Buie and Bus (1992)
[d] Mueller *et al.* (1992), Fernie (1983)

to the errors of measurement. Color-color plots are presented in Figs. 1 ($B-V$ vs. $V-R$) and 2 ($V-R$ vs. $R-I$); solar colors are also marked on the plot. The plots show no distinction between the Centaurs and the Kuiper Belt objects; furthermore, there is no evident clustering within these two groups. The colors in Table 6 can also be converted into relative spectral reflectances (i.e., original spectrum divided

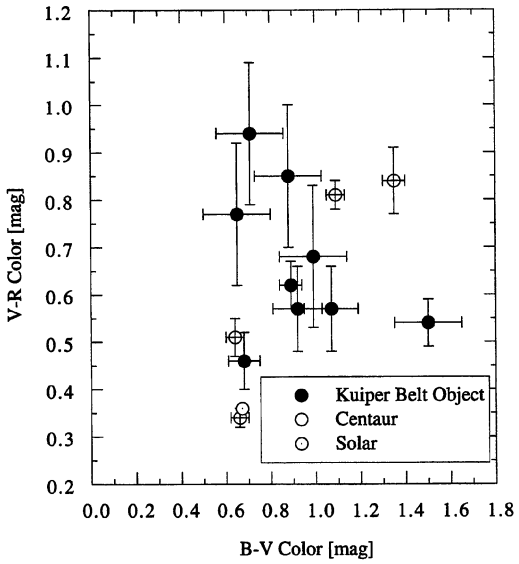

FIG. 1. $B-V$ color plotted against $V-R$ color for Centaurs (empty circles) and Kuiper Belt (filled circles) objects. The color of the Sun is marked.

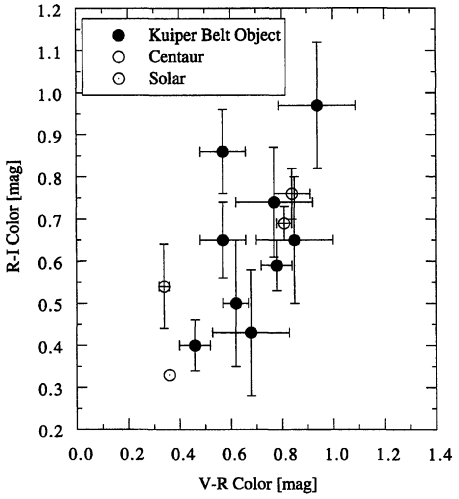

FIG. 2. $V-R$ color plotted against $R-I$ color for both Centaurs (empty circles) and Kuiper Belt (filled circles) objects. The color of the Sun is marked.

by solar spectrum) at the effective central wavelengths of the broadband filters. The $R-B$, $R-V$, and $R-I$ colors then yield relative reflectances normalized at the R filter through the equation

$$S_\lambda = 10^{0.4(c-c_s)}, \quad (1)$$

where S_λ is the normalized reflectance at the appropriate central wavelength, c is the color, and c_s is the solar color. The reflectances are plotted in Fig. 3. CCD spectra are available for Chiron and Pholus so these are plotted directly in Fig. 3 instead of the converted broadband colors. It is clear

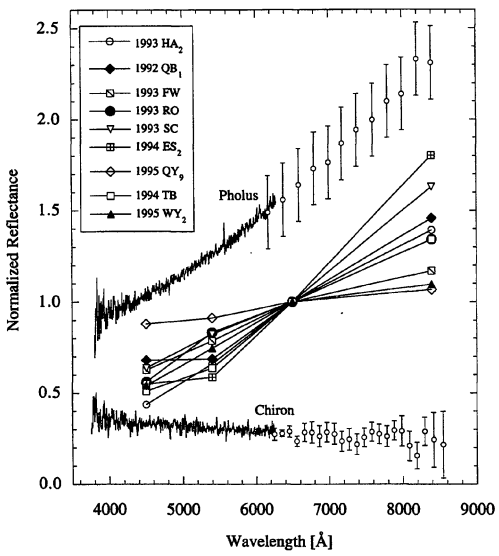

FIG. 3. Relative reflectances of the Kuiper Belt and Centaur objects. The reflectances are normalized at the R filter (6500 Å). The spectra of Chiron and Pholus have been offset for clarity, but the slopes of their reflectances are directly comparable with those of the Kuiper Belt objects. The spectrum of Pholus at $\lambda \geq 6200$ Å is taken from Fink *et al.* (1992).

TABLE 7. Color–color correlations.

Sample	Test	N^a	$r_x{}^b$	P^c
Kuiper Belt	B-V vs. V-R	9	0.3924	0.30
Kuiper Belt	V-R vs. R-I	9	0.5411	0.13
Centaurs	B-V vs. V-R	4	0.9188	0.08
Centaurs	V-R vs. R-I	3	0.9659	0.17
Kuiper Belt and Centaurs	B-V vs. V-R	13	0.1712	0.58
Kuiper Belt and Centaurs	V-R vs. R-I	12	0.5608	0.06

[a] Number of objects
[b] Linear correlation coefficient
[c] Probability of obtaining this correlation coefficient or one larger, purely by chance from uncorrelated data

that the spectral slopes of the Centaur and Kuiper Belt objects vary over a similarly wide range, and that Chiron and Pholus can be regarded as end members of the color distribution of these distant objects. This visual assessment is corroborated by a chi-squared test applied to both groups of objects: we find no statistical difference (at the 3σ level) between the color distributions of the Kuiper Belt and Centaur objects. This result is consistent with (but, of course, does not uniquely prove) a Kuiper Belt origin for the Centaurs.

4. DISCUSSION

4.1 Color–Color Relation

Broadband colors by themselves offer limited insight into surface composition, but a systematic correlation between different color indices would tend to suggest that the population can be characterized by a homogeneous surface composition. We tested for a linear correlation between $B-V$ and $V-R$, and between $V-R$ and $R-I$, for both the Centaurs and Kuiper Belt objects. Results from the tests are summarized in Table 7. As indicated in the table, there is no statistical evidence for linear correlations between the colors, either for each individual group or for both groups combined. These statistical tests echo the color diversity shown in Table 6 and Fig. 3.

4.2 Collisional Resurfacing

The Kuiper Belt objects show a very wide range of colors, from nearly solar ($V-R=0.46$, 1995 QY_9) to very red ($V-R=0.94$, 1994 ES_2). How can the color diversity be explained in the context of the steady reddening presumed to be caused by the omnipresent flux of cosmic rays? We advanced several possible explanations in Luu & Jewitt (1996). Here, we develop the idea that the observed color dispersion is caused by collisional resurfacing of the Kuiper Belt objects. In this model, the progressive global reddening caused by cosmic-ray bombardment of surface organics is countered by resurfacing due to impacts.

The stopping length for ~MeV cosmic rays is of order 1 m (Johnson *et al.* 1987). We suppose that impacts excavate material from beneath the irradiation mantle, and that this unirradiated material is optically less red and less dark than the surface mantle. The instantaneous color (and albedo) of the surface is then the result of the competition between progressive reddening by cosmic rays and stochastic resurfacing by less red, unirradiated material. An obvious analogy can be

drawn with the white ray systems observed on dark, atmosphereless bodies such as the Moon. The time scale for *in situ* growth of the irradiated mantle is estimated at $\tau_m \sim 10^{8\pm1}$ yr (Shul'man 1972). A spread of colors will result when the irradiation mantling time τ_m is of the same order as the global resurfacing time, τ_r. In the following section, we address the calculation of τ_r as a function of the size distribution of the likely impactors.

Assuming power-law size distributions, the timescales for collision between the largest objects in the Belt (diameter $D \geqslant 100$ km) are longer than the age of the solar system, but are $\sim 10^6$–10^8 yr between 100 km size and km-size bodies (Stern 1995). The known Kuiper Belt objects have inclinations in the range $0° \leqslant i \leqslant 30°$ and eccentricities $0 \leqslant e \leqslant 0.3$ (Jewitt *et al.* 1996). We take the velocity dispersion in the Belt as $\Delta V \sim V_K[2(e^2+i^2)]^{1/2} \sim 2$ km/s, where $V_K = 5$ km/s is the local Keplerian velocity. If we assume a density of 1000 kg m^{-3} for both a 1 km projectile and a 100 km target, the specific energy (projectile kinetic energy divided by the target mass) is

$$E_{\rm spec} \sim 2 \text{ J/kg}. \tag{2}$$

From laboratory experiments of low-velocity impacts on ice (impact velocity $V_i = 0.1$–0.7 km/s), the specific energy required for complete destruction of an ice target is estimated to be ~50 J/kg (Kawakami *et al.* 1983). Similar results are reached by Lange & Ahrens (1981) from experiments with water ice targets at $V_i \sim 1$ km/s. It is thus reasonable to assume that, in the Kuiper Belt, the impact of a 1 km projectile onto a 100 km target (in this case, ratio of projectile mass to target mass is 10^{-6}) results in cratering rather than complete target disruption.

Matsui *et al.* (1984) note that, in collisions involving low-strength targets (as material in the trans-Neptunian region is likely to be), the dissipation of kinetic energy is much enhanced compared to collisions involving compact and hard material. The escape velocity from a 100 km radius target is $V_e \sim 75$ m/s, giving $V_e/V_i \approx 0.04$. Collision experiments with impact velocities in the km/s range suggest that the fraction of impact energy that is translated into ejecta kinetic energy is ~1% (Fujiwara & Tsukamoto 1980; Davis & Ryan 1990). Theoretical and experimental investigations show that most of the mass displaced by impact leaves the crater at speeds much less than V_e, even for a 6 km/s impact into a hard (basaltic) target (Housen *et al.* 1983). Experiments by Hartmann (1985) indicate that the ejecta velocity distributions measured for impacts into particulate (regolith-like) targets are even more biassed towards subescape velocities. On the basis of these results, we expect that the bulk of the ejecta resulting from 2 km/s impacts onto 100 km scale Kuiper Belt objects should fall to the surface, creating a layer of fall-back debris around each impact crater. The impacts may still be net erosive (more mass escapes as ejecta than is delivered by the projectile), but the bulk of the displaced material falls back to the surface.

We examine this hypothesis using a simple Monte Carlo model to simulate the aging (i.e., reddening) versus cratering (resurfacing) process on a Kuiper Belt object. A detailed calculation is presently impossible, since the number density of cratering projectiles in the Kuiper Belt is not well known. Our objective is to establish the qualitative color response to resurfacing by impacts in order to assess resurfacing as the cause of the observed color diversity. The model assumes that the Kuiper Belt objects obey a power-law size distribution:

$$N_1(a)da = \Gamma a^{-q}\, da, \tag{3}$$

where $N_1(a)da$ is the number density of Kuiper Belt objects having radii in the range a to $a+da$, and Γ and q are constants. The normalization constant Γ is calculated from the statistics of 35,000 Kuiper Belt objects with radii $\geqslant 50$ km (Jewitt & Luu 1995), occupying a volume lying between 30 and 50 AU in radius and 10 AU in height. (Note that our recent work tends to increase the number of objects by a factor ~2, but the volume is also increased so that the impact rate derived remains unchanged.) We focus attention on power law size indices $q = 2.5$, 3.0, 3.5 because they are close to the indices seen among comet nuclei (Shoemaker & Wolfe 1982) and because current Kuiper Belt statistics suggest similar values (Jewitt *et al.* 1996). The collision rate is calculated from

$$n_c(a)da = N_1(a)\sigma \Delta V da, \tag{4}$$

where $n_c(a)da$ = number of collisions with projectiles in the size range a to $a+da$ per unit time, σ = target cross section, and ΔV = velocity dispersion (we neglect gravitational focusing). For definiteness, the projectiles are assumed to have radii a_p in the range $0.1 \leqslant a_p \leqslant 1$ km. The choice of upper limit chosen here does not materially affect the results since, given the power law size distributions, the larger projectiles are rare and thus contribute little to the impact rate. Using the population lower limit from Jewitt & Luu (1995), we calculate the collision time scale $\tau_r \sim 10^7$ yr for $q = 2.5$ and $\tau_r \sim 10^6$ yr for $q = 3.0$, compatible with the collision rates reported by Stern (1995). Reducing the lower projectile size limit from 0.1 km to 10 m leads to such high impact rates (e.g., $\tau_r \sim 10^4$ yr) that, given the adopted parameters in the model, the targets never have a chance to develop an irradiation mantle. On the other hand, the absence of numerous subkilometer comet nuclei may suggest that the abundance of such bodies is depleted in the Kuiper Belt.

We use the scaling law for cratering in ice (at 81 K) from Lange & Ahrens (1987):

$$\Pi_r \Pi_2^{0.31} = 0.05, \tag{5}$$

where Π_r and Π_2 are dimensionless parameters defined by

$$\Pi_r = r_c \left(\frac{\rho_p}{m_p} \right)^{1/3}, \tag{6}$$

$$\Pi_2 = 3.22 \frac{g a_p}{V_i^2} \tag{7}$$

In Eq. (6), r_c is the crater radius (m), m_p the projectile mass (kg), and ρ_p the projectile density (kg m^{-3}). In Eq. (7), g is the surface gravity of the target (m s^{-2}), a_p is the projectile radius (m), and V_i is the impact velocity (m s^{-1}). Equations

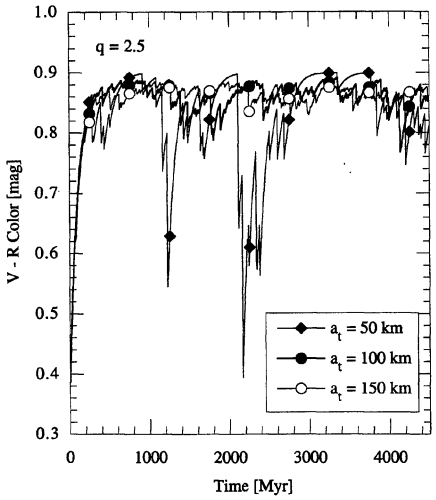

FIG. 4. Model colors of a Kuiper Belt target as a function of time, assuming $q=2.5$. The target radii are $a_t=50$, 100, and 150 km, and the projectile radii are $0.1\leqslant a_p\leqslant 1$ km.

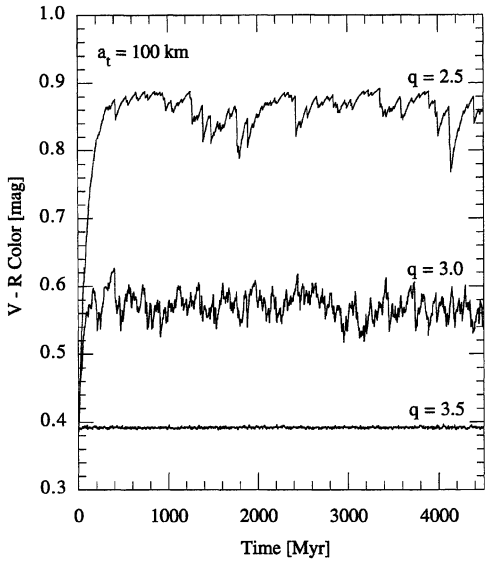

FIG. 5. Model colors of a 100 km radius Kuiper Belt object as a function of time. The upper, middle and bottom curves show models having size distributions $q=2.5$, $q=3.0$, and $q=3.5$, respectively. The projectile radii are $0.1\leqslant a_p\leqslant 1$ km.

(5)–(7) were originally determined for the impact velocity range 0.2 km/s $\leqslant V_i\leqslant$ 0.8 km/s, but we assume that the laws are applicable for our slightly larger velocities. We combine Eqs. (5)–(7), with $V_i=2$ km/s and $\rho_p=1000$ kg m^{-3}, to calculate the crater radius r_c (m) as a function of a_p:

$$r_c=6.7\times 10^2 a_p^{0.69} a_t^{-0.31}. \tag{8}$$

In Eq. (8), a_t is the target radius (a_t and a_p in m). The radius of the ejecta blanket is 10–50 times larger than the crater size (Housen *et al.* 1983). We conservatively take the radius of the ejecta blanket to be

$$r_{eb}=10 r_c. \tag{9}$$

We simulate the reddening of the target with

$$V-R=A\ \exp\left(\frac{-t}{B}\right)+C. \tag{10}$$

In Eq. (10), t is time measured in years while constants $A=-0.54$, $B=10^8$ yr, $C=0.90$ were determined by the boundary conditions $V-R=0.36$ at $t=0$ and $V-R\rightarrow 0.90$ as $t\rightarrow 10^8$ yr. (The $V-R=0.90$ boundary condition was assumed from the observed color range.) A 1000×1000 array was used to represent the surface of a 100 km body. We use a time step of 5×10^6 yr, this being sufficiently fine considering the slow growth of the irradiation mantle ($\sim 10^8$ yr). The global color is obtained by linearized averaging of $V-R$ over all pixels at each time step.

Sample results are plotted in Fig. 4. In the figure, the global $V-R$ color is shown as a function of time for various target sizes, assuming $q=2.5$. In the case of target radius $a_t=50$ km, the model reproduces the large color range observed among Kuiper Belt objects. For a given power-law size distribution, the model generally predicts smaller color excursions for the larger targets. These smaller excursions can simply be explained by the fact that the impacts, although relatively frequent, cover a proportionately smaller fraction of their surface and thus have reduced effect on the global color. The opposite situation applies to the smaller targets. The color thus depends on the fraction of target surface area a typical impact can resurface.

Figure 5 shows the effect of different power laws (collision timescales) on targets of the same size. In the three cases, the target radius is fixed at $a_t=100$ km, and q varies between 2.5 and 3.5. For each time scale, the surface gradually reddens, but with interruptions due to resurfacing impacts. When impacts are relatively rare (e.g., $q=2.5$), the surface reaches an equilibrium red color close to the saturation value with only small excursions due to localized resurfacing (upper curve in Fig. 5). Conversely, when the resurfacing impacts are frequent ($q=3.5$) the target never has enough time to grow red (lower curve). An intermediate color is produced by an intermediate collision timescale, whereby an equilibrium is reached between the occasional impacts and the steady reddening (middle curve). The model thus demonstrates qualitatively the asymptotic colors produced in the cases of very long or very short collision time scales.

The collisional resurfacing model makes several predictions:

(1) Because of the near-surface ice, recently resurfaced areas on a Kuiper Belt object should be of higher albedo than older areas blackened by cosmic-ray irradiation.

(2) There should be an inverse correlation between the albedo and the $V-R$ color index, i.e., low albedo objects should be redder than high albedo objects.

(3) For the same reason, if exposed surface volatiles are to be detected on these distant bodies, it will be on the recently resurfaced, spectrally less red objects.

(4) There is no one-to-one correlation between color and size, but larger objects as a group should show less scatter in their colors than the smaller objects. The reason is the fol-

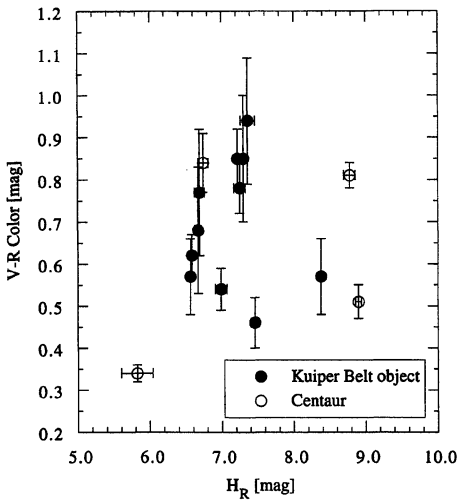

FIG. 6. $V-R$ color plotted against absolute magnitude H_R. No trend is apparent.

lowing. On a large target, individual impacts do not blanket a large fraction of the surface area so that a single color measurement is likely to sample an averaged color of red and neutral areas. On a small target, an individual impact can blanket a larger fraction of the surface, so a single-color measurement could be dominated by a red or neutral area (e.g., Fig. 4). Thus color measurements of small Kuiper Belt objects may, in general, show a larger dispersion than colors of large Kuiper Belt objects.

The above model is highly idealized in order to crystallize the idea that global color variations might result from a competition between cosmic-ray reddening and impact resurfacing. In the real case, cosmic-ray reddening of the optically active upper few mm may well occur on timescales short compared to the adopted 10^8 yr. On the other hand, micrometeorite "gardening" will rapidly recycle a thin upper layer of regolith (just as on the moon). Clearly, the relevant physical processes are complex and intertwined. Our intent here is less to attempt a detailed simulation of these processes than to demonstrate that the process might occur, provided the reddening and global resurfacing times are of the same order. The success of the models, plus the observation that the Moon has been at least locally resurfaced (e.g., the rays of Tycho crater), give us confidence that impact resurfacing may explain the measured color diversity in the Kuiper Belt. At the same time, we acknowledge that the resurfacing model is not unique. It is entirely possible, for example, that Kuiper Belt objects formed at a range of heliocentric distances and temperatures, and incorporated somewhat different elemental abundances due to selective capture of volatile ices. The different compositions alone might give rise to the observed color spread.

4.3 Color–Size Relation

Is there a correlation between the target size and color? The model described above predicts that (1) small Kuiper Belt objects exhibit a larger color dispersion than large objects, and (2) there is no one-to-one correlation between color and size, i.e., one cannot predict an object's color based on its size (see Fig. 4). We attempt to test these predictions by plotting the $V-R$ colors of the Kuiper Belt and the Centaur objects as a function of absolute magnitude (i.e., size) in Fig. 6. The figure shows no significant color-size correlation in the observed sample, and seems to bear out the latter prediction. However, we regard this result as inconclusive, given the fact that the sample size is small and consists of objects in a narrow (100–400 km) diameter range. A more rigorous test of the model predictions will require a larger sample with a wider diameter range.

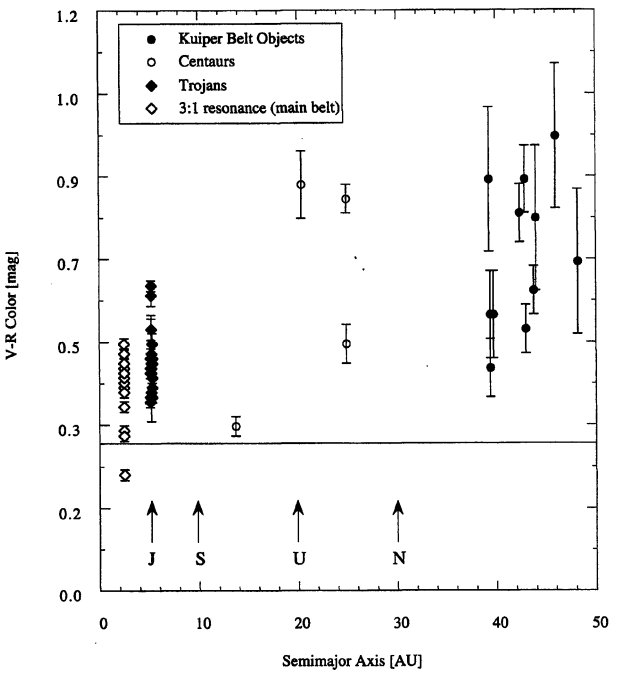

FIG. 7. $V-R$ color plotted against semimajor axis. The locations of the gas-giant planets are marked for reference. The horizontal line marks the solar $V-R$.

4.4 Color–Distance Relation

Color variations as a function of distance have been reported within the asteroid belt (cf. Gradie & Tedesco 1982; Gradie *et al.* 1989), and explained in terms of solar system chemical condensation models (e.g., Lewis 1974) and evolutionary processes (Bell *et al.* 1989; Cruikshank *et al.* 1996). In Fig. 7 we show the color distributions of the Trojan asteroids (semimajor axis a ~5.2 AU) and the 3:1 resonance main belt asteroids ($a=2.5$ AU), compared with the more distant objects from the present work. The 3:1 resonance asteroids are used here to represent the middle region of the main belt and no genetic relationship with the Centaurs or Kuiper Belt objects is implied. The large color dispersion among the Centaurs and Kuiper Belt objects prevents us from discerning any color gradient in the 20–45 AU region. However, as a group, the Kuiper Belt objects possess larger $V-R$ colors than the Jovian Trojans or main-belt asteroids.

4.5 Comparison with Other Solar System Objects

Over the last few years we have conducted a low-resolution optical spectroscopic survey of numerous small solar system bodies, including the nuclei of comets (Luu 1993), near-Earth asteroids (Luu & Jewitt 1989), and Trojan asteroids (Jewitt & Luu 1990). From these CCD spectra we have compiled a list of $V-R$ colors for comparison with the Centaurs and Kuiper Belt objects (the $V-R$ measurements are more numerous than any other color measurement). The colors were computed from S', the normalized reflectivity gradients of the spectra, by the relation

$$V-R=2.5\ \log\left(\frac{2+S'\Delta\lambda}{2-S'\Delta\lambda}\right), \tag{11}$$

where S' is in $\%/10^3$ Å, and $\Delta\lambda=\lambda_2-\lambda_1$ is the difference in effective wavelength (in 10^3 Å). The spectra varied slightly in the beginning and ending wavelengths, but all cover the 4000–7000 Å range and encompass the V and R bandpasses. Where both broadband photometry and CCD spectra are available (e.g., Pholus and Chiron), the "color" obtained from Eq. (11) and the broadband color are mutually consistent.

The $V-R$ histograms of the various types of objects are compared in Fig. 8. The histograms show that most solar system bodies exhibit colors redder than solar (solar $V-R=0.36$ in the Kron–Cousins filter system). Furthermore, the Centaurs and the Kuiper Belt objects exhibit the broadest range of colors, including the reddest colors seen among the small bodies of the solar system. In our target sample, the Centaur color range is $0.3\leqslant V-R\leqslant 0.8$, and the Kuiper Belt $0.4\leqslant V-R\leqslant 1.0$, as opposed to the $0.2\leqslant V-R\leqslant 0.6$ range seen in asteroids and comet nuclei.

The fact that the Kuiper Belt colors can only be matched by the Centaurs is probably the strongest observational argument for a common origin for both groups of objects. In view of the dynamical characteristics of the Centaurs, and the similarities between the two color distributions, the theoretical and observational evidence is in favor of a Kuiper Belt origin for the Centaurs. Finally, the unusual colors of these distant objects suggest primitive material indigenous to the outer solar system, e.g., irradiated organic-rich ices.

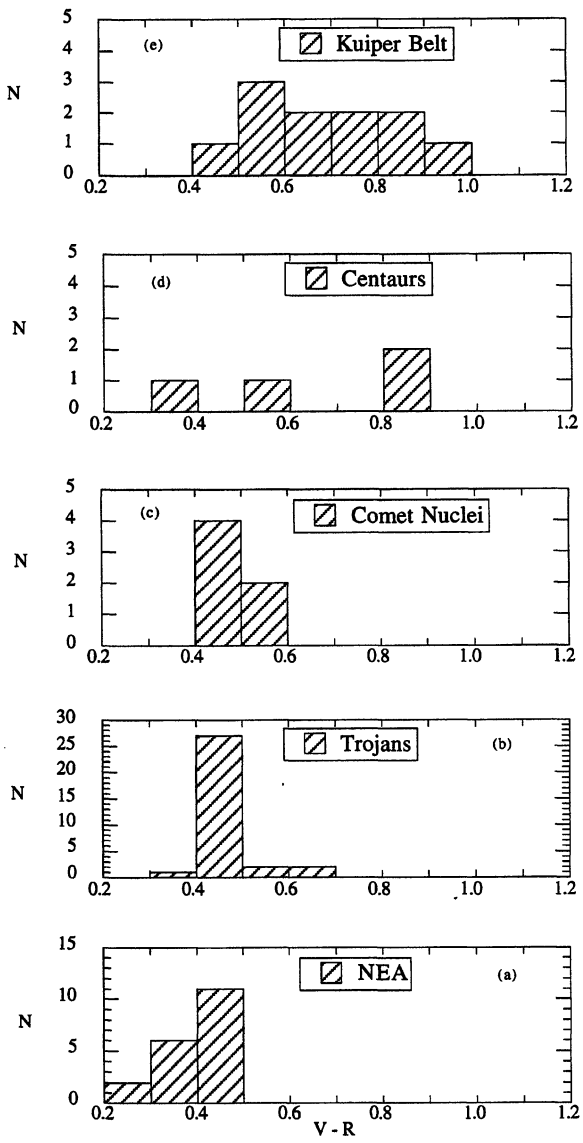

FIG. 8. Histograms of $V-R$ colors of several groups of solar system objects, with semimajor axis increasing from the bottom upward: (a) near-Earth asteroids, (b) Trojan asteroids, (c) comet nuclei, (d) Centaurs and (e) Kuiper Belt objects. The Centaurs and Kuiper Belt objects display the largest range of colors, including the reddest colors among the presented groups.

4.5.1 Kuiper Belt objects and nuclei of short-period comets

In contrast to the Centaurs and Kuiper Belt objects, the nuclei of short-period comets are believed to have blown off their irradiation mantles and are instead covered by nonvolatile "rubble mantles," formed by large particles too heavy to be ejected from the nucleus (see, e.g., Rickman *et al.* 1990). According to our small sample of known comet nuclei, the rubble mantles possess red colors similar to those of Trojan asteroids (which primarily belong to the P and D taxonomic classes). The dissimilar color distributions of the known comet nuclei and the Kuiper Belt objects suggest that rubble mantles and irradiation mantles have different reflectivities, perhaps due to the absence of long-term irradiation, and/or more intense solar heating. The rubble versus irradiation mantle dichotomy may perhaps explain the contrast between the Centaurs Chiron and Pholus. Chiron possesses a blue-neutral color (unique in the current distant object sample), and its near-IR spectrum is essentially featureless (Luu *et al.* 1994). On the other hand, Pholus is famous for its extremely red color, and its near-IR spectrum shows several absorption features (Davies *et al.* 1993; Luu *et al.* 1994; Cruikshank *et al.* 1996), which have been attributed to hydrocarbons. Chiron is also the only Centaur to exhibit cometary activity and thus should sport a fresh rubble mantle from steady outgassing (e.g., Luu & Jewitt, 1990, 1993). The presence of outgassing in Chiron and the lack of it in Pholus provides a simple, although non-unique, explanation for their contrast-

ing spectral properties. This interpretation further predicts that near-IR spectra of active comets will also be mostly featureless.

4.5.2 Kuiper Belt objects and Trojan asteroids

The Trojans are considered to be the most primitive of the known asteroid types (Bell *et al.* 1989). This is, in part, due to their larger heliocentric distance (compared to the main-belt asteroids) and hence smaller solar insolation. One might expect that irradiation mantles should also exist on these primitive asteroids. However, the optical colors presented in this paper suggest otherwise, and near-IR spectra of Trojans also reveal no organic features like those observed in Pholus (Luu *et al.* 1994). These results suggest that either (1) the Trojans were never able to build up an irradiation mantle, perhaps because their composition was not sufficiently ice rich, or (2) if they did, the organic features have been obliterated by solar heating (Cruikshank *et al.* 1996).

5. SUMMARY

(1) We have obtained broadband photometry of four of the six known Centaurs and 14 of the 36 Kuiper Belt objects known at the time of writing. The colors are redder than sunlight and vary over a range which far exceeds the color range of the main-belt asteroids and the (few) measured comet nuclei (Fig. 8).

(2) The preponderance of very red colors seen only among the Kuiper Belt and Centaur objects suggests a surface material which is either rare or not present on asteroids and known comet nuclei.

(3) There is no statistically significant difference between the Kuiper Belt and Centaur color distributions, compatible with (but not proving) a Kuiper Belt origin for the Centaurs.

(4) The large range of colors in the Kuiper Belt and Centaur objects is a surprising observational result in the context of the expected ubiquitous cosmic ray darkening and reddening of these bodies. It may suggest (a) the existence of more than one type of initial surface composition, or (b) the effects of time-dependent surface modification. While we specifically do not assert that collisional resurfacing is the agent responsible for the observed color range, we do claim that this mechanism must be considered if the reddening and resurfacing times are found to be comparable. Our hypothesis is non-unique, but makes several predictions that can be observationally tested.

We are thankful to the telescope operators and observatory support staff in Hawaii and Chile. DJ thanks NASA's Origins Of Solar Systems Program for support of this work.

REFERENCES

Asher, D. J., & Steel, D. I. 1993, MNRAS, 263, 179
Bell, J. F., Davis, D. R., Hartmann, W. K., & Gaffey, M. J. 1989, in Asteroids II, edited by R. P. Binzel, T. Gehrels, and M. S. Matthews (University of Arizona Press, Tucson), pp. 921–945
Bowell, E., Hapke, B., Domingue, D., Lumme, K., Peltoniemi, J., & Harris, A. 1989, in Asteroids II, edited by R. Binzel, T. Gehrels, and M. Matthews (University of Arizona Press, Tucson), pp. 524–556
Buie, M. W., & Bus, S. J. 1992, Icarus, 100, 288
Cruikshank, D. P., *et al.* 1996, Icarus (submitted)
Davies, J. K., Sykes, M. V., & Cruikshank, D. P. 1993, Icarus, 102, 166
Davis, D. R., & Ryan, E. V. 1990, Icarus, 83, 156
Duncan, M., Quinn, T., & Tremaine, S. 1988, ApJ, 328, L69
Fernie, J. D. 1983, PASP, 95, 782
Fink, U., Hoffman, M., Grundy, W., Hicks, M., & Sears, W. 1992, Icarus, 97, 145
Fujiwara, A., & Tsukamoto, A. 1980, Icarus, 44, 142
Gradie, J., & Tedesco, E. F. 1982, Science, 216, 1405
Gradie, J., Chapman, C. R., & Tedesco, E. F. 1989, in Asteroids II, edited by R. P. Binzel, T. Gehrels, and M. S. Matthews (University of Arizona Press, Tucson), pp. 316–335
Hahn, G., & Bailey, M. E. 1990, Nature, 348, 132
Hartmann, W. K. 1985, Icarus, 63, 69.
Hartmann, W., Tholen, D. J., Meech K. J., & Cruikshank, D. P. 1990, Icarus, 83,
Holman, M., & Wisdom, J. 1993, AJ, 105, 1987
Housen, K. R., Schmidt, R. M., & Holsapple, K. A. 1983, J. Geophys. Res., 88, 2485
Irwin, M., Tremaine, S., & Zytkow A. N. 1995, AJ, 110, 3082
Jewitt, D. C., & Luu, J. X. 1990, AJ, 100, 933
Jewitt, D. C., & Luu, J. 1995, AJ, 109, 1867
Jewitt, D. C., Luu, J. X., & Chen, J. 1996, AJ (in press)
Johnson, R. E., Cooper, J. F., Lanzerotti, L. J., & Strazzulla, G. 1987, A&A, 187, 889
Kawakami, S., Mizutani, H., Takagi, Y., Kato, M., & Kumazawa, M. 1983, J. Geophys. Res., 88, B7, 5806
Landolt, A. 1992, AJ, 104, 340
Lange, M. A., & Ahrens, T. J. 1981, Proc. Lunar Planet. Sci., 12B, 1667
Lange, M. A., & Ahrens, T. J. 1987, Icarus, 69, 506
Lewis, J. S. 1974, Science, 186, 440
Luu, J. 1993, Icarus, 104, 138
Luu, J. X., & Jewitt, D. C. 1989, AJ, 99, 1985
Luu, J., X., & Jewitt, D. 1990, AJ, 100, 913
Luu, J. X., & Jewitt, D. 1993, in Workshop on the Activity of Distant Comets, edited by W. F. Huebner, H. U. Keller, D. Jewitt, J. Klinger, and R. West (Southwest Research Institute, San Antonio), pp. 44–53
Luu, J. X., & Jewitt, D. C. 1996, AJ, 111, 499
Luu, J. X., Jewitt, D. C., & Cloutis, E. 1994, Icarus, 109, 133
Matsui, T., Waza, T., & Kani, K. 1984, J. Geophys. Res., 89 (Suppl. B), 700
Moore, M. H., Donn, B., Khanna, R., & A'Hearn, M. F. 1983, Icarus, 54, 388
Mueller, B. E. A., Tholen, D. J., Hartmann, W. K., & Cruikshank, D. P. 1992, Icarus, 97, 150
Oke, J. B., *et al.* 1995, PASP, 107, 375
Rickman, H., Fernández, J. A., & Gustafson, B. Å. S. 1990, A&A, 237, 524
Shoemaker, E. M., & Wolfe, R. F. 1982, in Satellites of Jupiter, edited by D. Morrison (University of Arizona Press, Tucson), pp. 277–339
Shul'man, L. M. 1972, in The Motion, Evolution of Orbits, and Origin of Comets, IAU Symp. 45, edited by Chebotarev *et al.* (Reidel, Dordrecht), p. 265
Stern, S. A. 1995, AJ, 110, 856
Williams, I. P., O'Ceallaigh, D. P., Fitzsimmons, A., & Marsden, B. G. 1995, Icarus, 116, 180